

Ultra-low frequency waves in the Hermean magnetosphere: On the role of the morphology of the magnetic field and the foreshock

E. Kallio¹, R. Jarvinen^{1,2}, S. Massetti³, T. Alberti³, A. Milillo³, S. Orsini³, E. De Angelis³, G. Laky⁴, J. Slavin⁵, J. M. Raines⁵ and T. I. Pulkkinen⁵

¹ Department of Electronics and Nanoengineering, School of Electrical Engineering, Aalto University, Espoo, Finland

² Finnish Meteorological Institute, Helsinki, Finland

³ National Institute of Astrophysics, Institute for Space Astrophysics and Planetology, INAF-IAPS, Rome, Italy

⁴ Space Research Institute, Austrian Academy of Sciences, Graz, Austria

⁵ Department of Climate and Space Sciences and Engineering, University of Michigan, Ann Arbor, MI, USA

Key points:

- Ultra-low frequency waves in Mercury's magnetosphere were investigated with a global hybrid model
- About 2-second period circularly polarized right-handed waves occur on closed field lines along BepiColombo's 1st Mercury flyby in the model
- The waves are generated on the hemisphere which is directly magnetically connected to the interplanetary magnetic field and to the foreshock

This is the author manuscript accepted for publication and has undergone full peer review but has not been through the copyediting, typesetting, pagination and proofreading process, which may lead to differences between this version and the [Version of Record](#). Please cite this article as doi: [10.1029/2022GL101850](https://doi.org/10.1029/2022GL101850).

This article is protected by copyright. All rights reserved.

Abstract

Ultra-low frequency (ULF) waves have been observed in the Mercury's magnetosphere by the Mariner 10 and MESSENGER missions. The observed ~ 2 s (~ 0.6 Hz) period waves in the magnetic field are proposed to be generated by dynamic processes in the Mercury's magnetosphere. We investigate the Hermean ULF waves with a global hybrid model. We found evidence for ~ 2 -s circularly polarized right-handed waves in Mercury's magnetosphere at the closest approach of BepiColombo mission's first Mercury flyby in the model. The most intense wave power occurs on the dawn side closed magnetic field lines. These waves were found to be generated on the hemisphere which is magnetically directly connected to the interplanetary magnetic field on the dayside and to the foreshock region. It is therefore possible that the generation mechanism of these waves is associated with the precipitating ion flux or with the wave activity in the foreshock region.

1 Introduction

Characterization of the properties of the Ultra-low frequency (ULF) waves in planetary magnetospheres provides a way to investigate magnetospheric dynamics and the properties of the magnetosphere, such as the density of magnetospheric plasma. The dynamics of Mercury's magnetosphere are anticipated to have unique properties as it has an intrinsic magnetic field that is weak compared to that of the Earth, but strong compared to the other terrestrial planets and the interplanetary magnetic field (IMF).

A unique magnetic feature at Mercury is that the relatively low conductivity of the crust and mantle results in a rapid (timescale of minutes) transmission of magnetic field perturbations from the high-altitude solar wind interaction and magnetosphere down to the outermost layers of the iron core. These perturbations include large-scale compressions and rarefactions [Slavin et al., 2014; Jia et al., 2015], field-aligned currents [Janhunen and Kallio, 2004; Anderson et al., 2014] and ULF waves [Southwood, 1997; James et al., 2016]. Hence, in many respects Mercury appears as a 2000 km radius perfectly conducting iron sphere overlaid by a weakly electrically conducting crust and mantle.

Observations from Mariner 10 flybys, as well as those by the MErcury Surface, Space ENvironment, GEochemistry and Ranging, MESSENGER (Solomon et al., 2007), mission showed that there are waves around Mercury at various frequencies [Le et al., 2013; Romanelli et al., 2020]. In analogy of the Earth's magnetosphere, some of the observed ULF waves were suggested to be Kelvin-Helmholtz waves [Boardsen et al., 2010], associated with field line resonance (FLR) events [Russell, 1989; James et al., 2019] or some kinetic instabilities [Kim et al., 2015]. However, it has been pointed out that the Mariner 10 ULF wave event has a clear compressional component, which indicates that they are not simple standing waves [Southwood, 1997]. The role of the plasma content at high-altitudes and the nature of the reflection of these waves near Mercury's highly conducting core interface must also be considered. Furthermore, the observed ~ 1 Hz waves have been proposed to be quasi-trapped [Boardsen et al., 2009]. Similar transient phenomena to those found in the Earth foreshock (e.g., Zhang et al., 2022) may exist at Mercury in one way or another.

The first observation of \sim second scale ULF waves was during near closest approach of the first Mariner 10 Mercury encounter [Russell, 1989]. These ~ 2 -s periodic waves were initially attributed to be FLRs, i.e., standing Alfvén waves [Russell, 1989]. Later, it was suggested that the “ringing” of the Hermean magnetosphere could be caused by small-amplitude compressional ULF waves [Glassmeier et al., 2004]. As the frequency of the observed waves was relatively close to the proton gyrofrequency, ion kinetic effects associated with ion cyclotron resonance or Bernstein waves have been suggested to play a role [Boardsen et al., 2009; 2012]. However, it should be noted that no Na^+ or other heavy planetary ion cyclotron waves have been observed in the Mariner 10 or MESSENGER magnetic field observations presumably due to their large gyroradii [Boardsen & Slavin, 2007]. The BepiColombo

mission provides a new opportunity to measure the Hermean solar wind interaction including ULF waves with several Mercury flybys happening prior to the orbit insertion in Dec 2025 [Milillo et al., 2020; Mangano et al., 2021].

In this paper, the ULF waves at Mercury are investigated with a global hybrid model, in which ions are modelled as particles. The simulation setup is the same as that recently used to investigate ULF waves in the Hermean foreshock [Jarvinen et al., 2020a]. We show that circularly polarized waves can exist in Mercury's magnetosphere on closed field lines at the closest approach of BepiColombo's first flyby (MFB1), on the dawn side near the foreshock.

The paper starts with introduction to the basic properties of the hybrid model and the simulation run. Following the analysis of the properties of the observed ULF waves, we suggest a possible origin of the observed waves by examining the global morphology of the magnetic field, especially, near the foreshock. We conclude by comparing the observations with the simulation results.

2 Model description

The ULF waves are investigated with a 3-dimensional hybrid simulation where ions are modelled as particles while electrons form a massless charge neutralizing fluid. The model was recently used to investigate ULF waves in the Hermean [Jarvinen et al., 2020a], Venusian [Jarvinen et al., 2020b] and Martian [Jarvinen et al., 2022] foreshocks.

We use a Mercury-centered coordinate system similar to the Mercury Solar Orbital (MSO) system, defined as the x axis pointing towards the Sun, z axis being parallel to the normal vector of Mercury's orbital plane, and y axis completing the right-handed system. All upstream solar wind and IMF parameters remain constant throughout the simulation. The upstream solar wind densities and temperatures were similar to that in the previous foreshock study [Jarvinen et al., 2020a]: $n(\text{H}^+) = 73 \text{ cm}^{-3}$, $n(\text{He}^{++}) = 2.92 \text{ cm}^{-3}$ ($= 0.04 \times 73 \text{ cm}^{-3}$), $T(\text{H}^+) = 1.7 \times 10^5 \text{ K}$, $T(\text{He}^{++}) = 3.5 \times T(\text{H}^+)$. Motivated by the solar wind parameters measured during MFB1 [Orsini et al., 2022], the upstream solar wind speed was assumed to be relatively slow and flowing in the $-x$ direction ($\mathbf{U}(\text{H}^+) = \mathbf{U}(\text{He}^{++}) = [U_x, U_y, U_z] = [-320 \ 0 \ 0] \text{ km/s}$) i.e., the aberration due to the orbital motion was not taken into account. The upstream IMF was set to $[-10, 8, 5] \text{ nT}$. The strength of the magnetic dipole was set to 195 nT R_M^3 ($R_M = 2439.7 \text{ km}$) and the dipole was at $[0, 0, 484] \text{ km}$ [Anderson et al., 2011]. The size of the simulation box was $x = [-10, 6] R_M$, $y = [-8, 12] R_M$, $z = [-8, 8] R_M$. The size of the Cartesian cell was $R_M / 15 \sim 163 \text{ km}$, the time step was 10 ms , and each cell contained on average 178 macroparticles. The planet was assumed to have a perfectly conducting core with a radius of 1800 km and an insulating layer (a mantle) above it (see Jarvinen et al., 2020a, for details).

The wave analysis was made by adding 144 “virtual detectors” to the simulation, along MFB1 trajectory on October 1, 2021. These detectors recorded particles and macroscopic plasma parameters during the run at every simulation time step (10 ms). Macroscopic plasma parameters (Fig. 1) and fields in the simulation domain were saved at $t = 300 \text{ s}$ to investigate the morphology of 3D magnetic field lines that provide global context for the particle measurements (see e.g., Milillo et al., 2020; Orsini et al., 2021; Orsini et al. 2022). As the trajectory resembles the orbit of the Mariner 10's 1st Mercury flyby, when $\sim 2 \text{ s}$ ULF waves were observed, and the MESSENGER's 1st Mercury flyby (ULF waves observed on January 14, 2008), we can compare our results with those from the previous missions. Fig. 1 shows an overview of the Hermean solar wind interaction environment and the MFB1 trajectory in the model. The perpendicular bow shock is clearly identified in the upper hemisphere of the figure by a sudden density enhancement. Density fluctuations are found on the parallel and quasi parallel side of the foreshock region on the dawn side

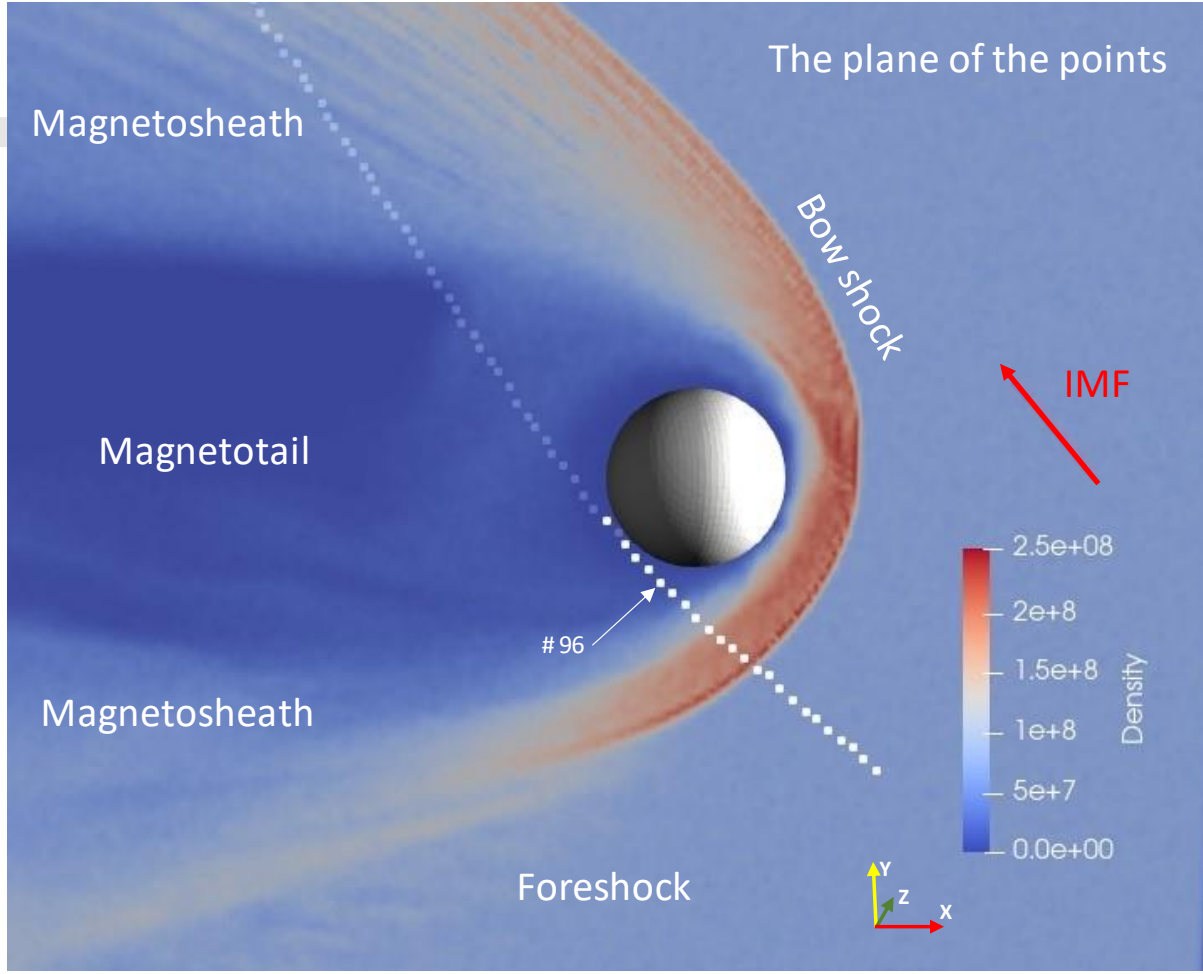


Figure 1. An overview of the plasma properties. The color shows the total ion density [m^{-3}] (H^+ and He^{++} ions) on a plane close to the 141 “virtual detectors” positioned along the center of the simulation cells near the orbit of MFB1. From small to large virtual detector numbers, they cover the nightside dusk magnetosheath, the magnetotail, the dayside dawn magnetosheath, and finally the solar wind on the foreshock side. The red long vector shows the orientation of the IMF. The position (#96) which is analyzed in detail is shown with a white arrow. The small red, yellow and green arrows show the used MSO coordinate system.

3 Properties of the ULF waves

Figure 2 shows the magnetic field values in the magnetosphere at the point $[-0.37, -1.03, -0.57]$ R_M (point #96) during 100 s period. According to a spectral analysis of the total magnetic field, there is a peak at frequency $f_{ULF} = 0.62$ Hz, i.e., at period $T_{ULF} = 1.6$ s. Furthermore, these waves contain a wave packet with a modulating period of about 20 – 30 s, especially, in the B_x and B_z MSO components (Fig. 2a and 2c).

The minimum variance analysis (MVA) for the time period 310–320 s shows that the waves are quite circularly polarized (Figs. 2e-f). The eigenvalues of the magnetic field are $[l_1, l_2, l_3] = [65.538, 62.654, 3.3225]$ nT^2 , i.e., variations in the perpendicular direction are more than an order of magnitude stronger than in the parallel (compressional) direction. The angle between the eigenvector $\mathbf{e}_3 = [-0.095884, -0.98874, 0.11491]$ and the mean direction of the magnetic field in the analyzed time range, $\mathbf{B}^0 (= [-0.41618, -0.86807, 0.27063]$ nT , $|\mathbf{B}| = 103.6$ nT) was $\sim 158^\circ$ implying that the angle between the

Author Manuscript

wave \mathbf{k} vector and the ambient magnetic field is $\sim 22^\circ$. The hodogram in Fig. 2e, where the magnetic field points out of the plane, shows counterclockwise motion indicating a right-handed wave in the simulation frame.

Detailed determination of the wavelength of the 1.6-s waves is complicated, as the waves propagate in 3D space. However, based on fluctuations of the 3D magnetic field lines, variations of the magnetic field along a line in the direction of \mathbf{e}_3 and variations in the time evolution of the magnetic field on 2D planes (see Movie S1 in Supporting Information S1), the wavelength (l_{ULF}) is of the order of 600 – 800 km. This range corresponds to phase speed ($= l_{\text{ULF}} / T_{\text{ULF}}$) in the range of 375 – 500 km/s. In the simulation time interval [250 350] s, in turn, the Alfvén velocity is between 568 km/s and 894 km/s with the average velocity being 708 km/s. These Alfvén speeds are, therefore, relatively close to the estimated phase speed of the 1.6-s waves taking into account the possible inaccuracies in the wavelength estimation.

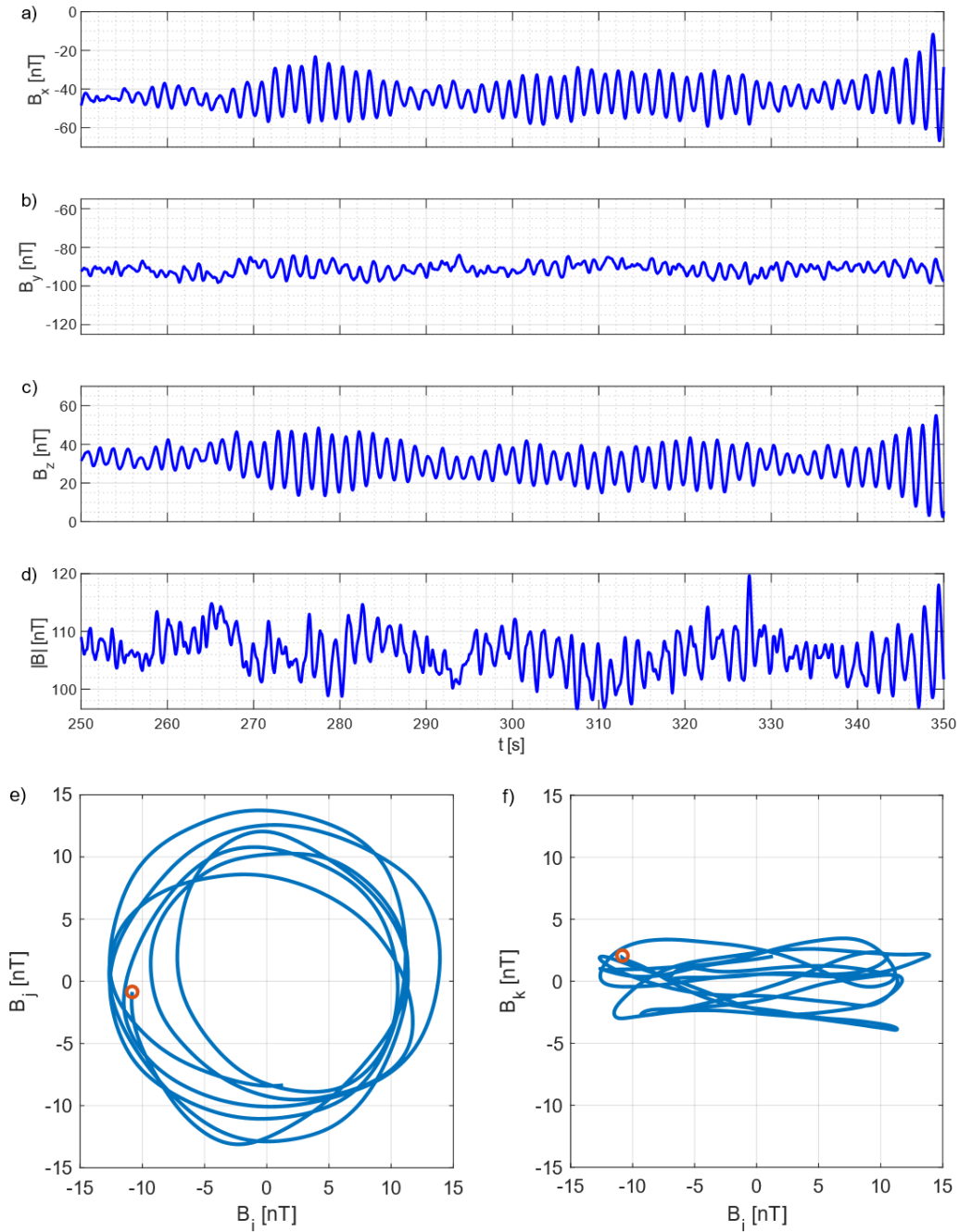


Figure 2. ULF waves in Mercury's magnetosphere at the point #96. a) B_x , b) B_y , c) B_z , and d) total B in the MSO coordinates during $t = 250 - 350$ s. The scale in panels a) – c) is the same (70 nT). e) – f) MVA of the magnetic field at #96 in the period of $t = 310 - 320$ s. The right-hand coordinate system unit vectors \mathbf{i} , \mathbf{j} , and \mathbf{k} are the maximum, intermediate, and minimum variance directions in the simulation coordinate system, respectively. Panel e) shows the hodogram of the magnetic field on the plane of the maximum (i) and intermediate (j) variance directions when the mean magnetic field value is subtracted. Panel f) represents the hodogram on the plane of the maximum(i) and minimum(k) variance directions. The red circles show the beginning of the time series.

4 Morphology of the magnetic field and the foreshock region

The relation of the waves in Fig. 2 to the Hermean global magnetosphere is then further examined in Fig. 3. The morphology of the magnetic field is assessed by starting field line tracing along the flyby trajectory at the virtual detector points. Fig. 3a shows the magnetic field lines connected to the virtual detector points #51([-4.83, 5.17, 1.17] R_M) - #107([1.10, -2.37, -0.77] R_M). The field lines are derived at $t = 300$ s from the start of the simulation.

The two first analysis points shown in Fig. 3a (#51, #52([-4.77, 5.03, 1.10] R_M)) are in the dusk magnetosheath, where the IMF magnetic field lines are draped around the southern hemisphere and finally, they form the IMF field lines upstream of the bow shock (c.f. field lines #51 and #52 at the bottom right corner).

The field lines #53([-4.70, 4.90, 1.03] R_M) - #78([-2.37, 1.50, 0.10] R_M) flow through the southern magnetic tail lobe. These open magnetic field lines, i.e., lines with only one footpoint connected to the planet, are connected to the southern hemisphere (the footpoints are behind the planet in Fig. 3a and thus not visible).

The magnetic field line #79([-2.23, 1.37, 0.03] R_M) is the first closed one with both footpoints connected to the planet. The last closed magnetic field line along the flyby trajectory is line #100([0.17, -1.57, -0.63] R_M) on the dawn side. The trajectory between points #79 - #100 is therefore in the closed magnetic field line region.

Finally, the first open field line on the dawn side is the point #101([0.30, -1.70, -0.63] R_M), which is connected to the northern hemisphere. As the plasma density color coding along the field line indicates, the field line moves through the high density magnetosheath. The first magnetically disconnected point is #126([3.63, -4.43, -1.10] R_M). This field line bends around the northern hemisphere to the dusk magnetosheath (not shown). After that point, the trajectory is in the solar wind and the associated magnetic field lines have solar wind topology and flow to the dusk magnetosheath.

The properties of the field lines on the dawn side around point #96 are investigated in more detail in Fig. 3b. The color coding after point #99([0.03, -1.43, -0.63] R_M) shows how these magnetic field lines go through the high density magnetosheath while the plasma density is low on the closed magnetic field lines. Note also a small “twisting” on the closed magnetic field line on the northern hemisphere. The magnetic field lines on the dawn side connected to the northern hemisphere are in the region where the IMF is relatively parallel to the bow shock normal, i.e., on the foreshock region.

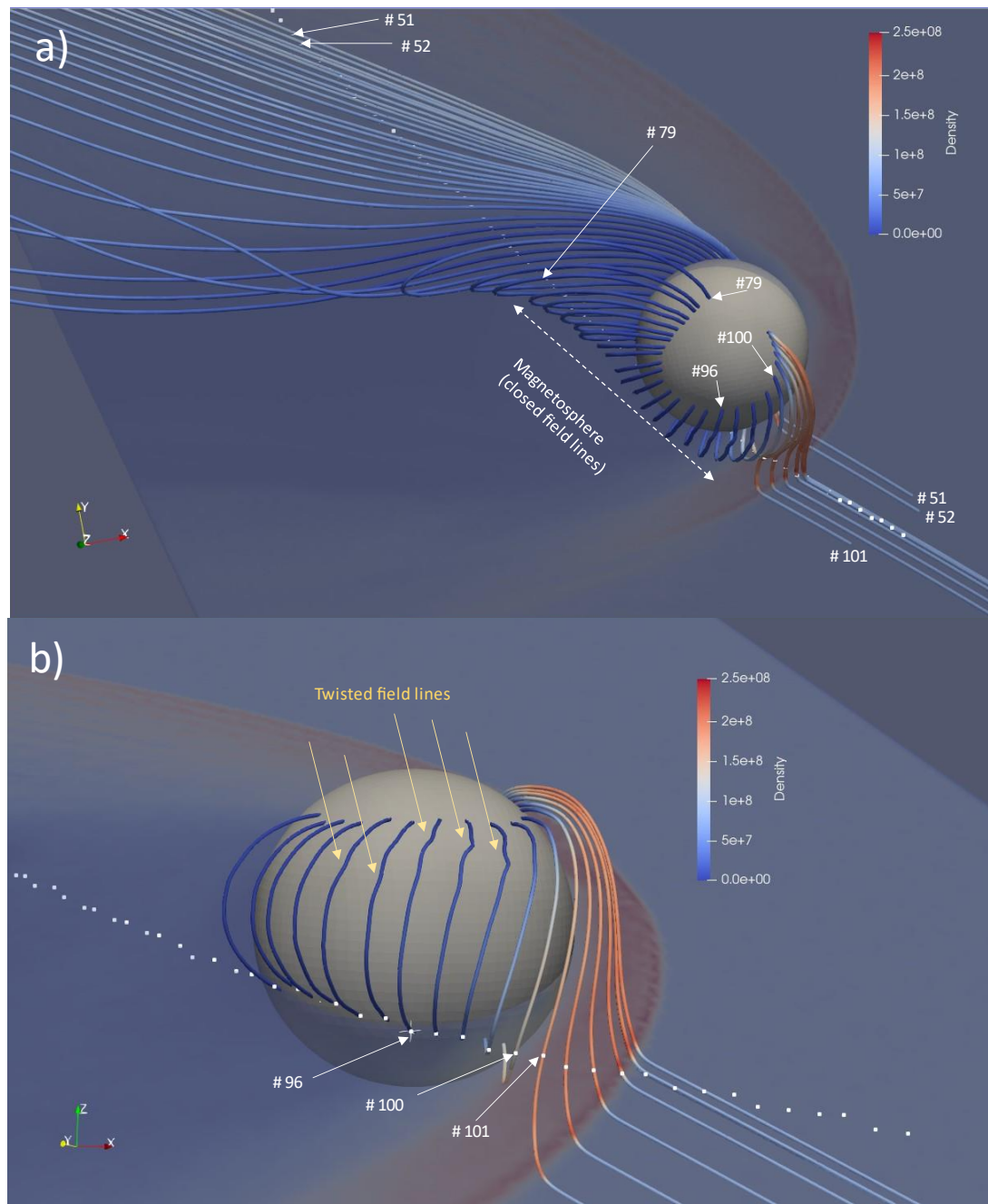


Figure 3. Morphology of the magnetic field lines around Mercury. The points #51 – #52 are in the magnetosheath, points #53 – #78 in the southern magnetic tail lobe, the points #79 – # 100 in the closed magnetic field line region and the magnetic field lines after that are connected to the northern hemisphere. The color shows the total plasma density on an approximate MFB1 plane (Fig. 1). Panel a) shows the magnetic field lines connected to the points #51 – #107 and b) to the points #90 – #107. The waves at the point #96 were investigated earlier in Fig. 2.

Fig. 4 shows the global scale morphology of the magnetic field near Mercury in more detail in Fig. 4. The figure shows the magnetic field B_y component on two planes and on a spherical shell 360 km above the Hermean surface; this altitude is still clearly within the magnetosphere. Magnetic field lines connecting to the planetary surface are also shown. As the dipole field value in the $y = 0$ plane is

zero, the B_y component on this plane is caused by the IMF and is a measure of the planet's interaction with the solar wind.

Figs. 4a) and b) demonstrate clear wave activity on the Northern hemisphere around the north magnetic cusp, which is located on the dusk sector. No clear wave activity can be detected on the southern hemisphere. When the positions of the magnetic cusps are determined by calculating the angle (α) on the planet's surface between the surface normal and the magnetic field, the north magnetic cusp ($\alpha \sim 180^\circ$) is located near z-axis at high latitudes, within the bounds set by in MESSENGER observations [Winslow et al., 2012; Raines et al., 2022]. The south magnetic cusp ($\alpha \sim 0^\circ$) instead is shifted toward dawn to lower latitude ($\sim 40^\circ$ S) in the analyzed solar wind parameters. The shifting and twisting of the position of the cusp from the $y = 0$ plane is caused partly by the IMF B_y component (see e.g., Kallio et al., 2008, Figs. 2 and 3) and partly by the off-centered magnetic dipole.

Note that clear wave activity can also be seen near the dawn equator both on the surface of the shell and as a fluctuations of the magnetic field (Fig. 4a). While the snapshot shown in Fig. 4 cannot be used to identify the propagation of the waves, we can draw conclusions from the time series of B_y on the $y = 0$ plane. These data suggests that the waves originate from near the planet on the northern dayside hemisphere, from where they propagate tailward, then toward the center of the tail and continue to the southern hemisphere (see Movie S1 in Supporting Information S1).

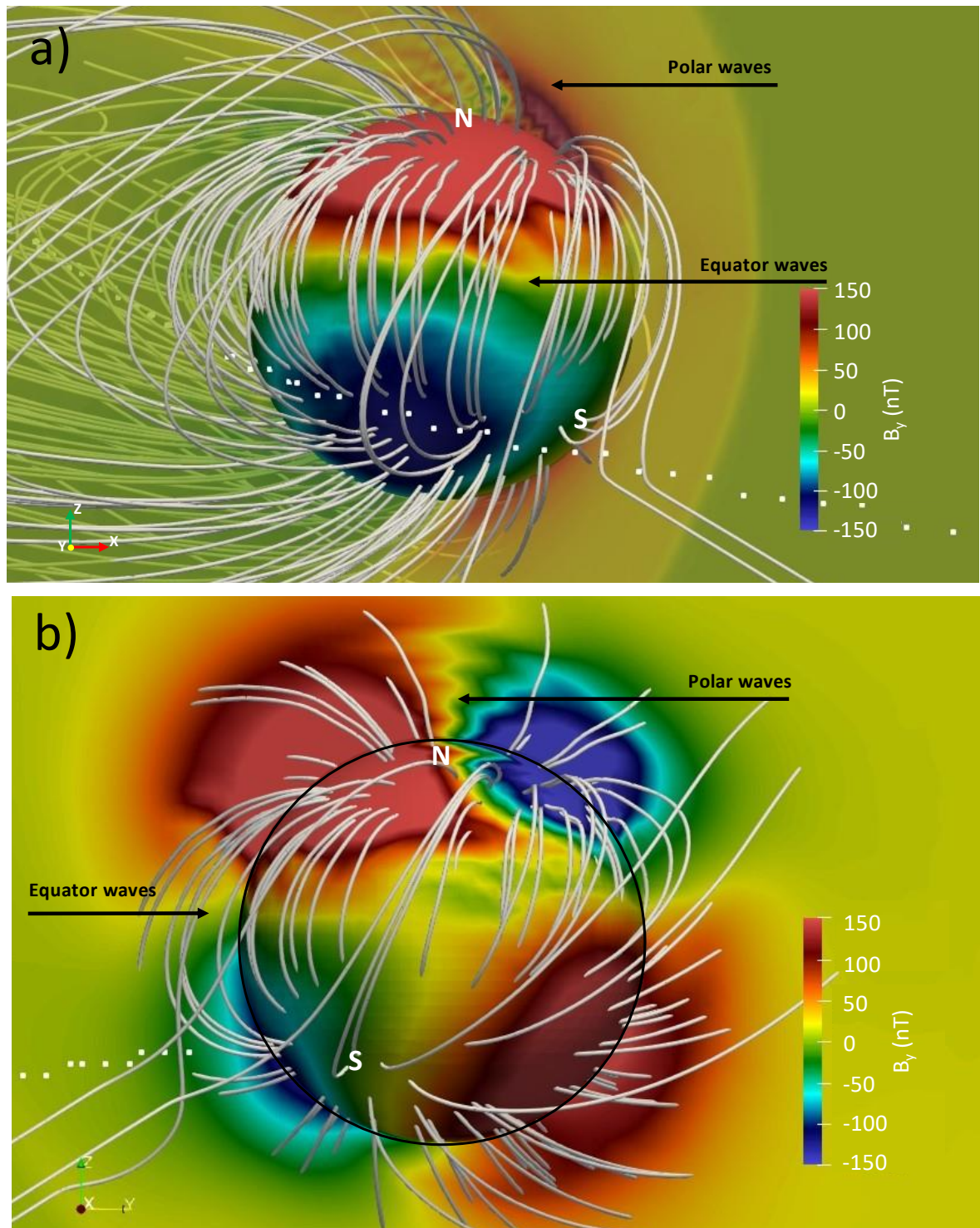


Figure 4. The magnetic field B_y (nT) component a) on the noon-midnight meridian plane ($y = 0$) viewed from the dawn side and b) on the terminator plane ($x = 0$) viewed from the Sun. The B_y is also shown in both panels on a spherical shell of a radius 2800 km. The white lines represent 500 magnetic field lines which tracing were started on the planet surface. The white dots show the position of the virtual detectors. The white arrows show the position where waves can be identified on the north polar region and slow variations on the dawn equator. The approximate position of the north and the south magnetic

cusps are shown by letters N and S, respectively. A black circle is added in b) to show clearly the position where the planet surface crosses the $x = 0$ plane.

5 Discussion and conclusions

In this paper, ULF waves in the Hermean magnetosphere with period ~ 2 s were studied with a hybrid model. The analyzed region was chosen to be along the orbit of MFB1, which provides insight of the plasma regions sampled by the spacecraft. We find that ULF waves are formed naturally in a global hybrid simulation even when stationary upstream parameters are used as boundary conditions.

Although this study showed some basic properties of the ULF waves in the simulation, the study leaves open the question of their generation mechanism. It has been suggested that the ion-ion instability could be a potential origin for the observed ULF waves at Mercury (see e.g., Boardsen et al., 2012, 2015, and references therein). As the hybrid simulation does not include planetary ions, planetary ions cannot be the source of the ULF waves seen in the simulation. In the analyzed region, the average magnetic field was ~ 106 nT corresponding to gyro periods of 0.6 s and 1.2 s for H^+ and He^{++} ions, respectively. Both time scales are shorter than the observed 1.6 s waves in the closed field line region.

To examine the 1.6 s wave association with FLR, we calculate the time it takes for an Alfvén wave to propagate along the field line between its footpoints on the planet's surface. The length of the magnetic field line #96 is $\sim 6,400$ km. We estimate the propagation time by integrating over the field line in distance steps dl_i and summing the propagation time, dt_i , over each time step using $\sum_i dt_i = \sum_i dl_i / v_{Alfvén,i}$, where the local Alfvén velocity at the step i is $v_{Alfvén,i}$. This gives a surface-to-surface propagation time of ~ 12 seconds, which is over 7 times longer than the period of the 1.6 s wave. Moreover, the bounce time is larger than this because the waves are bounced from the surface of the iron core. Thus, if the observed wave would result from FLR, it would be at the 7th harmonic frequency.

One possible cause for the hemispherical asymmetry is that the intrinsic magnetic field is larger on the surface on the northern hemisphere than on the southern hemisphere, because the magnetic dipole is centered 484 km $\sim 0.2 R_M$ from the origin towards the northern hemisphere in the simulation. The asymmetric intrinsic magnetic field is not, however, a necessary requirement for all ULF waves in the Hermean magnetosphere, as clear ULF wave activity was found also in the hybrid model run [Jarvinen et al., 2020a] in which the dipole was placed at the center of the planet.

The hemispherical asymmetry may also be related to the direction of the IMF B_x component. In the analyzed solar wind condition with negative B_x , the northern hemisphere was magnetically connected to the IMF because. If, instead, there would have been a strong positive IMF B_x component, the southern hemisphere would have been magnetically connected to the IMF [Kallio and Janhunen, 2004]. Earlier hybrid and analytical models have shown that the hemisphere magnetically connected to upstream is also the region of intense precipitation of solar wind particles to Mercury's surface (see e.g., Kallio and Janhunen, 2003; Massetti et al., 2003). Moreover, the IMF connected on the surface on the dawn side passed through the quasi-parallel bow shock (e.g., Figs. 1 and 3), where ULF waves have been observed (see e.g., Romanelli et al., 2020) and identified from hybrid simulations [Jarvinen et al., 2020a].

One should note that also the IMF B_z plays an important role in magnetosphere's dynamics. When the IMF points away from the Sun ($B_x < 0$), reconnection will shift to occurring just tailward of the cusps when IMF is northward ($B_z > 0$). This adds additional mass from the solar wind to the Dungey cycle. This IMF configuration was the case in the analysed simulation. However, in the southward B_z case ($B_z < 0$) the site for magnetopause reconnection will tend to be around the sub-solar region. In such way southward B_z adds energy, momentum, magnetic flux and mass to Mercury's Dungey cycle.

Finally, we note that the simulation contains also longer period 10 - 20 s variations or modulations of the magnetic field, as can be seen at point #96 (c.f. in Fig. 2d) and, for example, at point #97 closer to the magnetopause. The ~16 s ULF waves, which have been suggested to be associated with Kelvin Helmholtz instabilities, have frequently been identified in MESSENGER's magnetic field measurements [Boardsen et al., 2010; Sundberg et al., 2012]. For example, MESSENGER observed a close correlation between Kelvin-Helmholtz waves along the afternoon local time magnetopause (exactly where BepiColombo entered the magnetosphere), the appearance of bursts of Na⁺ ions, and ULF waves (see Sundberg et al., 2012, Figs 2 – 6; Gershman et al., 2015).

An especially interesting question is the possible role of the precipitating particles and/or foreshock waves for the generation of the ULF waves in Mercury's magnetosphere. Ion measurements during MFB1 have revealed rapid flux fluctuations within just a few seconds near the closest approach [Harada et al., 2022]. However, until now, no ULF wave observations have been published from MFB1. This is not unexpected, as BepiColombo's magnetic field measurements during the flyby were limited by the cruise configuration of the mission [Heyner et al., 2021; Baumjohann et al., 2020]. BepiColombo flybys and orbit phase beginning in 2026 provide unique new possibilities to investigate ULF waves at Mercury [Milillo et al., 2020; Mangano et al., 2021].

In summary, we show hybrid simulation results on ULF waves generated in the Hermean magnetosphere with ~2-s period consistent with observations by the Mariner 10 and MESSENGER missions. We show that the waves were generated on the hemisphere with direct connection to the IMF through the foreshock region, pointing to the foreshock region as a potential source for the wave activity.

Acknowledgments

The work was supported by the Academy of Finland (Decision No. 310444). J. A. Slavin's contributions were supported by NASA Grant 80NSSC21K005.

Data Availability Statement

Hybrid simulations were performed using the RHybrid simulation platform, which is available under an open-source license by the Finnish Meteorological Institute
<https://doi.org/10.5281/zenodo.7391464>

References:

- Anderson et al. (2011). The Global Magnetic Field of Mercury from MESSENGER Orbital Observations, *Science*, 333, 6051, 1859-1862. <https://doi.org/10.1126/science.1211001>
- Anderson, B. J., Johnson, C. L., Korth, H., Slavin, J. A., Winslow, R. M., Phillips, R. J., & Solomon, S. C. (2014). Steady-state field-aligned currents at Mercury, *Geophysical Research Letters*, 41, 7444–7452, <https://doi.org/10.1002/2014GL061677>.
- Baumjohann, W., Matsuoka, A., Narita, Y. et al. (2020). The BepiColombo–Mio Magnetometer en Route to Mercury, *Space Sci. Rev.*, 216, 125, <https://doi.org/10.1007/s11214-020-00754-y>.
- Boardsen, S. A., B. J. Anderson, M. H. Acuña, J. A. Slavin, H. Korth, and S. C. Solomon (2009). Narrow-band ultra-low-frequency wave observations by MESSENGER during its January 2008 flyby through Mercury’s magnetosphere, *Geophysical Research Letters*, 36, L01104, <https://doi.org/10.1029/2008GL036034>.
- Boardsen, S. A., T. Sundberg, J. A. Slavin, B. J. Anderson, H. Korth, S. C. Solomon, and L. G. Blomberg (2010). Observations of Kelvin-Helmholtz waves along the dusk-side boundary of Mercury’s magnetosphere during MESSENGER’s third flyby, *Geophysical Research Letters*, 37, L12101, <https://doi.org/10.1029/2010GL043606>.
- Boardsen, S. A., and J. A. Slavin (2007). Search for pick-up ion generated Na⁺ cyclotron waves at Mercury, *Geophysical Research Letters*, 34, L22106, <https://doi.org/10.1029/2007GL031504>.
- Boardsen, S. A., J. A. Slavin, B. J. Anderson, H. Korth, D. Schriver, and S. C. Solomon (2012). Survey of coherent ~1 Hz waves in Mercury’s inner magnetosphere from MESSENGER observations, *Journal of Geophysical Research*, 117, A00M05, <https://doi.org/10.1029/2012JA017822>.
- Boardsen, S. A., E.-H. Kim, J. M. Raines, J. A. Slavin, D. J. Gershman, B. J. Anderson, H. Korth, T. Sundberg, D. Schriver, and P. Travnicek (2015). Interpreting ~1 Hz magnetic compressional waves in Mercury’s inner magnetosphere in terms of propagating ion-Bernstein waves, *Journal of Geophysical Research: Space Physics*, 120, 4213–4228, <https://doi.org/10.1002/2014JA020910>.
- Gershman, D. J., J. M. Raines, J. A. Slavin, T. H. Zurbuchen, T. Sundberg, S. A. Boardsen, B. J. Anderson, H. Korth, and S. C. Solomon (2015). MESSENGER observations of multiscale Kelvin-Helmholtz vortices at Mercury, *Journal of Geophysical Research: Space Physics*, 120, <https://doi.org/10.1002/2014JA020903>.
- Glassmeier, K.-H., D. Klimushkin, C. Othmer, and P. Mager (2004). ULF waves at Mercury: Earth, the giants, and their little brother compared, *Adv. Space Res.*, 33, 1875–1883, <https://doi.org/10.1016/j.asr.2003.04.047>.
- Harada, Y., Aizawa, S., Saito, Y., André, N., Persson, M., Delcourt, D., et al. (2022). BepiColombo Mio observations of low-energy ions during the first Mercury flyby: Initial results, *Geophysical Research Letters*, 49, e2022GL100279, <https://doi.org/10.1029/2022GL100279>.

Heyner, D., Auster, H.-U., Fornaçon, K.-H. et al. (2021). The BepiColombo Planetary Magnetometer MPO-MAG: What Can We Learn from the Hermean Magnetic Field?, *Space Science Reviews*, 217, 52, <https://doi.org/10.1007/s11214-021-00822-x>.

James, M. K., E. J. Bunce, T. K. Yeoman, S. M. Imber, and H. Korth (2016). A statistical survey of ultra-low-frequency wave power and polarization in the Hermean magnetosphere, *Journal of Geophysical Research: Space Physics*, 121, 8755–8772, <https://doi.org/10.1002/2016JA023103>.

James, M. K., Imber, S. M., Yeoman, T. K., & Bunce, E. J. (2019). Field line resonance in the Hermean magnetosphere: Structure and implications for plasma distribution. *Journal of Geophysical Research: Space Physics*, 124, 211–228, <https://doi.org/10.1029/2018JA025920>.

Janhunen, P., and E. Kallio (2004). Surface conductivity of Mercury provides current closure and may affect magnetospheric symmetry, *Annales Geophysicae*, 22, 1829–1837, <https://doi.org/10.5194/angeo-22-1829-2004>.

Jarvinen, R., M. Alho, E. Kallio, T. I. Pulkkinen (2020a). Ultra-low frequency waves in the ion foreshock of Mercury: A global hybrid modeling study, *Monthly Notices of the Royal Astronomical Society*, stz3257, <https://doi.org/10.1093/mnras/stz3257>.

Jarvinen, R. M. Alho, E. Kallio and T. I. Pulkkinen (2020b). Oxygen Ion Escape from Venus is modulated by Ultra-Low-Frequency Waves, *Geophysical Research Letters*, 47, 11, <https://doi.org/10.1029/2020GL087462>.

Jarvinen, R., Kallio, E., & Pulkkinen, T. I. (2022). Ultra-low frequency foreshock waves and ion dynamics at Mars. *Journal of Geophysical Research: Space Physics*, 127, e2021JA030078, <https://doi.org/10.1029/2021JA030078>.

Jia, X., J. A. Slavin, T. I. Gombosi, L. K. S. Daldorff, G. Toth, and B. van der Holst (2015). Global MHD simulations of Mercury's magnetosphere with coupled planetary interior: Induction effect of the planetary conducting core on the global interaction, *Journal of Geophysical Research: Space Physics*, 120, 4763–4775, <https://doi.org/doi:10.1002/2015JA021143>.

Kallio, E., and P. Janhunen (2003). Solar wind and magnetospheric ion impact on Mercury's surface, *Geophysical Research Letters*, 30, 17, 1877, <https://doi.org/10.1029/2003GL017842>.

Kallio, E., and P. Janhunen (2004). The response of the Hermean magnetosphere to the interplanetary magnetic field, *Adv. Space Res.*, Vol. 33, 2176–2181, [https://doi.org/10.1016/S0273-1177\(03\)00447-2](https://doi.org/10.1016/S0273-1177(03)00447-2).

Kallio, E., S. Barabash, P. Janhunen and R. Jarvinen (2008). Magnetized Mars: Transformation of Earth-like magnetosphere to Venus-like induced magnetosphere, 56, Issue 6, Pages 823–827, *Planetary and Space Science*, <https://doi.org/10.1016/j.pss.2007.12.005>.

Kim, E.-H., J. R. Johnson, E. Valeo, and C. K. Phillips (2015). Global modeling of ULF waves at Mercury, *Geophysical Research Letters*, 42, 5147–5154, <https://doi.org/10.1002/2015GL064531>.

Le, G., Chi, P. J., Blanco-Cano, X., Boardsen, S., Slavin, J. A., & Anderson, B. J. (2013). Upstream ultra-low frequency waves in Mercury's foreshock region: MESSENGER magnetic field observations. *Journal of Geophysical Research: Space Physics*, 118, 2809–2823, <https://doi.org/10.1002/jgra.50342>.

Mangano, V. et al. (2021). BepiColombo Science Investigations During Cruise and Flybys at the Earth, Venus and Mercury, *Space Sci. Rev.* 217, <https://doi.org/10.1007/s11214-021-00797-9>.

Masetti, S., S. Orsini, A. Milillo, A. Mura, E. De Angelis (2003). Mapping of the cusp plasma precipitation on the surface of Mercury, *Icarus* 166(2), 229, <https://doi.org/10.1016/j.icarus.2003.08.005>.

Milillo, A. et al. (2020). Investigating Mercury's Environment with the Two-Spacecraft BepiColombo Mission, *Space Science Reviews*, Vol. 216, Article No: 93, <https://doi.org/10.1007/s11214-020-00712-8>.

Orsini, S. et al. (2021). SERENA: particle instrument suite for Sun-Mercury interaction insights on-board BepiColombo, *Space Science Reviews*, Vol. 216, <https://doi.org/10.1007/s11214-020-00787-3>.

Orsini, S., Milillo, A., Lichtenegger, H. et al. (2022). Inner southern magnetosphere observation of Mercury via SERENA ion sensors in BepiColombo mission. *Nat Commun* 13, 7390. <https://doi.org/10.1038/s41467-022-34988-x>.

Raines, J. M., N. M. Staudacher, R. M. Dewey, P. J. Tracy, C. M. Bert, M. Sarantos, D. J. Gershman, J. M. Jasinski, C. F. Bowers, E. Fisher and J. A. Slavin (2022). Proton precipitation in Mercury's northern magnetospheric cusp, *Journal of Geophysical Research: Space Physics*, <https://doi.org/10.1029/2022JA030397>.

Romanelli, N., DiBraccio, G., Gershman, D., Le, G., Mazelle, C., Meziane, K., et al. (2020). Upstream ultra-low frequency waves observed by MESSENGER's magnetometer: Implications for particle acceleration at Mercury's bow shock, *Geophysical Research Letters*, 47, <https://doi.org/10.1029/2020GL087350>.

Russell, C. T. (1989). ULF waves in the Mercury magnetosphere, *Geophysical Research Letters*, 16, 1253–1256, <https://doi.org/10.1029/GL016i011p01253>.

Slavin, J. A., DiBraccio, G. A., Gershman, D., Imber, S., Poh, G. K., Raines, J., & Solomon, S. C. (2014). MESSENGER observations of Mercury's magnetosphere under extreme solar wind conditions. *Journal of Geophysical Research: Space Physics*, 119, 8087–8116, <https://doi.org/10.1002/2014JA020319>

Solomon, S. C., R. L. McNutt, Jr., R. E. Gold, and D. L. Domingue (2007). MESSENGER Mission Overview, *Space Sci Rev.*, 131: 3–39. <https://doi.org/10.1007/s11214-007-9247-6>.

Southwood, D. J. (1997). The magnetic field of Mercury, *Planetary and Space Science*, 45, 1, 113-117, [https://doi.org/10.1016/S0032-0633\(96\)00105-5](https://doi.org/10.1016/S0032-0633(96)00105-5).

Sundberg, T., S. A. Boardsen, J. A. Slavin, B. J. Anderson, H. Korth, T. H. Zurbuchen, J. M. Raines, and S. C. Solomon (2012). MESSENGER orbital observations of large-amplitude Kelvin-Helmholtz waves at Mercury's magnetopause, *Geophysical Research Letters*, 117, A04216, <https://doi.org/10.1029/2011JA017268>.

Winslow, R. M., C. L. Johnson, B. J. Anderson, H. Korth, J. A. Slavin, M. E. Purucker, and S. C. Solomon (2012). Observations of Mercury's northern cusp region with MESSENGER's Magnetometer, *Geophysical Research Letters*, 39, L08112, <https://doi.org/10.1029/2012GL051472>.

Zhang, H., Zong, Q., Connor, H., Delamere, P., Facskó, G., Han, D., Hasegawa, H., Kallio, E., Kis, Á., Le, G., Lembège, B., Lin, Y., Liu, T., Oksavik, K., Omid, N., Otto, A., Ren, J., Shi, Q., Sibeck, D., Yao, S. (2022). Dayside Transient Phenomena and Their Impact on the Magnetosphere and Ionosphere, *Space Science Reviews*, 218:40, <https://doi.org/10.1007/s11214-021-00865-0>.